

Polarization modulation instability in a nonlinear fiber Kerr resonator

JULIEN FATOMÉ^{1,2,3*}, BERTRAND KIBLER¹, FRANÇOIS LEO⁴, ABDELKRIM BENDAHMANE¹, GIAN-LUCA OPPO⁵, BRUNO GARBIN^{2,3,6}, STUART G. MURDOCH^{2,3}, MIRO ERKINTALO^{2,3} AND STÉPHANE COEN^{2,3}

¹Laboratoire Interdisciplinaire Carnot de Bourgogne, UMR 6303 CNRS Université Bourgogne Franche-Comté, Dijon, France

²Department of Physics, The University of Auckland, Private Bag 92019, Auckland 1142, New Zealand

³The Dodd-Walls Centre for Photonic and Quantum Technologies, New Zealand

⁴OPERA-Photonique, Université Libre de Bruxelles, CP 194/5, 50 Av. F. D. Roosevelt, B-1050 Brussels, Belgium

⁵SUPA and Department of Physics, University of Strathclyde, Glasgow G4 0NG, Scotland, European Union

⁶Université Paris-Saclay, CNRS, Centre de Nanosciences et de Nanotechnologies, 91120, Palaiseau, France

*Corresponding author: Julien.Fatome@u-bourgogne.fr

Received XX Month XXXX; revised XX Month, XXXX; accepted XX Month XXXX; posted XX Month XXXX (Doc. ID XXXXX); published XX Month XXXX

We report on the experimental and numerical observation of a polarization modulation instability (PMI) process occurring in a nonlinear fiber Kerr resonator. This phenomenon is phased-matched through the relative phase detuning between the intracavity fields associated with the two principal polarization modes of the cavity. Our experimental investigation is based on a 12-m-long fiber ring resonator in which a polarization controller is inserted to finely control the level of intra-cavity birefringence. Depending on the amount of birefringence, the temporal patterns generated via PMI are found to be either stationary or to exhibit a period-doubled dynamics. Experimental results are in good agreement with numerical simulations based on an Ikeda map for the two orthogonally polarized modes. Our study provides new insights into the control of modulation instability in multimode Kerr resonators. © 2020 Optical Society of America

<http://dx.doi.org/10.1364/OL.99.099999>

Modulation instability (MI) is a nonlinear phenomenon characterized by the exponential growth and evolution of periodic perturbations on top of an intense continuous-wave (cw) landscape [1, 2]. Underpinned by a phase-matched parametric process, it is associated with a transfer of energy from a narrow pump frequency component to a pair of sidebands arranged symmetrically around the pump. In single-pass optical fiber propagation, MI can be naturally phase-matched through a balance between anomalous group-velocity dispersion and Kerr

nonlinearity [1, 2]. In contrast, more general phase-matching conditions are possible in the context of passive Kerr resonators, such as fiber ring cavities, because of the crucial role played by the system's boundary conditions [3–5]. Various configurations of MI have been investigated in that context, including MI in the normal dispersion regime, MI via bichromatic or incoherent driving, as well as competition between MI and Faraday or period-doubled (P2) instabilities [6–12]. Moreover, at variance with single-pass propagation, MI in Kerr resonators can lead to the emergence of stationary periodic (Turing) patterns; such patterns are now understood to be intimately related to temporal cavity solitons and microresonator optical frequency combs [13–16].

Birefringence, and the nonlinear coupling between the polarization components of light, is also known to contribute to the phase-matching of parametric processes. This enables the manifestation of polarization MI (PMI) and the emergence of vector temporal patterns [17–19]. In driven resonators, PMI has only been investigated theoretically so far [20–22], but recent demonstrations of orthogonally-polarized dual comb generation in microresonators are sparking a renewed interest in this process [23]. In this Letter, we report on the direct experimental observation of PMI in a passive Kerr resonator. Our experimental test-bed is based on a normally dispersive fiber ring cavity that incorporates a polarization controller for adjustment of the intra-cavity birefringence. Birefringence gives rise to a relative phase detuning between the two orthogonal polarization modes of the cavity, which in turn affects the frequency shift of the PMI sidebands. We also find that birefringence can lead to period-doubled (P2) dynamics, characterized by a two round-trip cycle. Our experimental results are in good agreement with theoretical predictions and numerical simulations based on an iterative two-component Ikeda map.

The experimental setup is displayed in Fig. 1(a). It consists of a $L = 12\text{-m}$ long passive fiber ring cavity with a finesse F of about 27, mainly built out of a normally dispersive spun fiber. The fiber exhibits normal group-velocity dispersion $\beta_2 = 56 \text{ ps}^2/\text{km}$, and a nonlinear coefficient $\gamma = 6.5 \text{ /W/km}$. It is important to note that spun fibers are manufactured with a fast spinning of the preform during the drawing stage (here with a spatial period of 5 mm). In these conditions, most residual geometric distortions and anisotropies are averaged out, and the fiber can be considered isotropic. To prevent any additional source of bending-induced birefringence, the fiber was also carefully off-spooled and wound directly on our experimental board with a large diameter of about 50 cm. We estimate that this causes a birefringence Δn no greater than 10^{-8} [24], which can be neglected in our experiments.

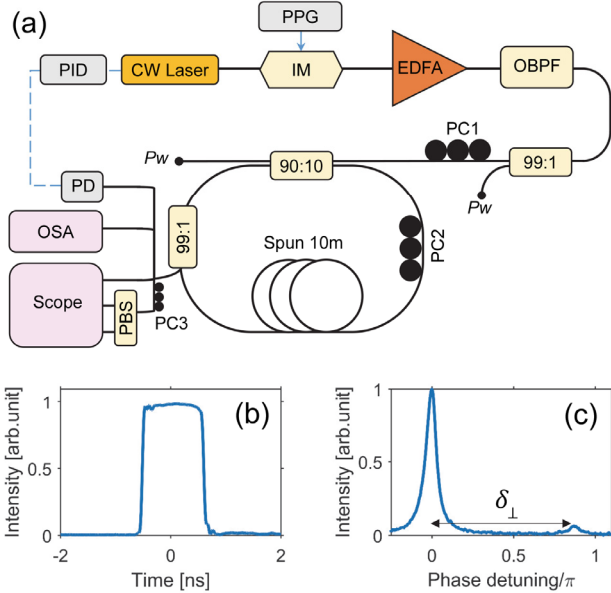


Fig. 1. (a) Experimental setup. PPG: pulse pattern generator, IM: intensity modulator, PC: polarization controller, EDFA: erbium doped fiber amplifier, OBPF: optical bandpass filter, PBS: polarization beam splitter, OSA: optical spectrum analyzer, PID: proportional integral derivative system, PD: photodetector, PW: power-meter. (b) Input pulse profile. (c) Linear resonances of the cavity.

Our fiber cavity is coherently-driven with a 1552.4 nm-wavelength cw laser (linewidth < 1 kHz), intensity-modulated to generate 1.1-ns square pulses [see Fig. 1(b)]. These pulses have a repetition rate of 17.54 MHz, matching the free-spectral range of our cavity. Intensity modulation enables increased peak driving power levels, while also circumventing stimulated Brillouin scattering [2]. The driving pulses are amplified by means of an erbium-doped fiber amplifier (EDFA) before injection into the cavity. At each round-trip, the driving field is superimposed on the intracavity signal through a 90:10 coupler made of standard single mode fiber (SMF28). A 99:1 SMF tap-coupler is also included to extract a part of the intra-cavity field for analysis. The output signal is characterized both spectrally and temporally, using respectively an optical spectrum analyzer (OSA) and a real-time 50-GHz bandwidth oscilloscope coupled to 70-GHz fast photodetectors.

Polarization management of this experiment is achieved by means of three polarization controllers (PC). First, the state of polarization (SOP) of the driving field is controlled (PC1) before the

input coupler in order to predominately excite one of the polarization modes of the fiber ring. Second, a polarization controller mounted directly onto the fiber cavity (PC2) is used to finely tune the level of intra-cavity birefringence through local mechanical stresses. This enables fine adjustments of the relative linear cavity round-trip phase shift δ_{\perp} between the two polarization modes of the cavity over the full $[-\pi, \pi]$ range; we measure this quantity by observing the linear cavity resonances while scanning the laser wavelength [see Fig. 1(c)]. Note that the laser wavelength can also be locked at a fixed detuning δ_0 from a resonance through a proportional-integral-derivative (PID) feedback loop. Finally, at the output of the system, a polarization beam splitter (PBS), preceded by a third polarization controller (PC3), is used to analyze individually the two polarization components of the intracavity field.

To model our experiment, we take advantage of the quasi-isotropic nature of our fiber, and describe propagation along the cavity with two coupled nonlinear Schrödinger equations. Denoting as $u^{(n)}(z, t)$ and $v^{(n)}(z, t)$ the circular polarization components of the intracavity electric field envelope during the n^{th} round trip [2], the fields evolution obeys

$$\begin{cases} \partial_z u^{(n)} = -i\frac{\beta_2}{2} \partial_{tt}^2 u^{(n)} + i\gamma' (|u^{(n)}|^2 + 2|v^{(n)}|^2) u^{(n)} \\ \partial_z v^{(n)} = -i\frac{\beta_2}{2} \partial_{tt}^2 v^{(n)} + i\gamma' (|v^{(n)}|^2 + 2|u^{(n)}|^2) v^{(n)}. \end{cases} \quad (1)$$

Here, z represents the propagation distance within the cavity, t is time expressed in a delayed reference frame, and the effective nonlinearity coefficient $\gamma' = (2/3)\gamma$ [2]. To form a map, these equations are completed by boundary conditions to describe coherent superposition between the intra-cavity field and the driving field at each roundtrip. This is expressed in terms of the linear polarization components, $E_x = (u + v)/\sqrt{2}$ and $E_y = -i(u - v)/\sqrt{2}$, as:

$$\begin{cases} E_x^{(n+1)}(0, t) = (1 - \alpha)E_x^{(n)}(L, t)e^{-i\delta_0} + \sqrt{\theta(1 - \varepsilon)}E_x^{(\text{in})} \\ E_y^{(n+1)}(0, t) = (1 - \alpha)E_y^{(n)}(L, t)e^{-i(\delta_0 + \delta_{\perp})} + \sqrt{\theta\varepsilon}E_x^{(\text{in})}. \end{cases} \quad (2)$$

Here the coefficient $\alpha = \pi/F = 0.116$ represents half of the total power loss per round-trip and $\theta = 0.1$ is the input coupling coefficient. Finally, for the sake of simplicity, we assume the driving field to be linearly polarized (along x) with a finite extinction ratio ε ($\varepsilon \ll 1$) so as to account for realistic experimental conditions. This means that both circular components are almost evenly excited at the input of the cavity. Below, we refer to the driving power $P_{\text{in}} = |E_x^{(\text{in})}|^2$ in terms of the normalized quantity $X = \gamma' L \theta P_{\text{in}} / \alpha^3$.

In order to highlight the key role of the birefringence in dissipative cavity PMI, we first discuss numerical results obtained by looking for steady-state solutions of the vector Ikeda map, Eqs. (1)–(2), for a range of relative detuning δ_{\perp} . We use parameters matching those used in the experiment, namely a driving power $X = 28$ (corresponding to 10 W peak driving power), a normalized linear detuning $\Delta = \delta_0/\alpha = 8$, and a finite polarization extinction-ratio between the linear components of the driving $\varepsilon = 10^{-3}$. The pseudo-color plot in Fig. 2(a) shows optical spectra obtained from our simulations. We can clearly observe the presence of intra-cavity MI, with the generation of sidebands and several harmonics around the central driving frequency for a range of values of δ_{\perp} . The strong dependence of the sidebands' position on the cavity birefringence clearly reveals the vector nature of the underlying process, and also that the sidebands are associated with PMI. We can notice that the

plot exhibits an overall “umbrella shape,” which repeats with a period of π in δ_{\perp} . No PMI is observed for δ_{\perp} very close to 0, i.e., for isotropic conditions, possibly due to the competing influence of the symmetry breaking instability that exists in such a case [20, 25, 26]. For other values of δ_{\perp} , the PMI sidebands move away from the pump as δ_{\perp} increases, until they eventually disappear for $\delta_{\perp} \bmod \pi > 0.8\pi$. We attribute this extinction to a decrease in the PMI gain. The optimum angular frequency of the PMI process, Ω_{opt} , can be well approximated by the following phase-matching condition, that expresses a balance between chromatic dispersion, linear detuning, birefringence, and intra-cavity power (P):

$$\Omega_{\text{opt}}^2 \frac{\beta_2 L}{2} - (\delta_{\perp} \bmod \pi + \delta_0) + \gamma' PL = 0 \quad (3)$$

Note that, for δ_{\perp} close to zero, this phase-matching condition corresponds to the isotropic PMI discussed in Ref. [20]. Since $\gamma' PL - \delta_0$ is relatively small in Eq. (3), the expression for the optimum PMI frequency can be further simplified as:

$$\Omega_{\text{opt}} = \sqrt{\frac{2[\delta_{\perp} \bmod \pi]}{\beta_2 L}} \quad (4)$$

The expression above, represented with circles in Fig. 2(a), clearly highlights the role of birefringence in this process.

In Fig. 2(b), we show a concatenation of experimental spectra measured at the output port of the 99:1 tap coupler in the same conditions as the numerical results of Fig. 2(a). The relative detuning δ_{\perp} was adjusted step-by-step by means of the intra-cavity PC2 while the detuning was kept locked at $\Delta = 8$. One can observe a good qualitative agreement between simulations and experiments. In particular, the repeating “umbrella” shape is clearly visible, as are the well separated, far detuned, and narrow sidebands corresponding to PMI. We must note an additional region of parametric gain around $\Omega_{\text{opt}}/2$, present in both the numerical and experimental spectra. We attribute this to a second-order vectorial four-wave mixing process between the linearly polarized pump wave and the first orthogonally-polarized sideband. Figure 3(a) presents a further comparison of the position of the first-order PMI sidebands obtained numerically (stars), analytically [dashed curves, Eqs. (3) and (4)], and experimentally (circles) as a function of the relative detuning δ_{\perp} . The agreement is very good.

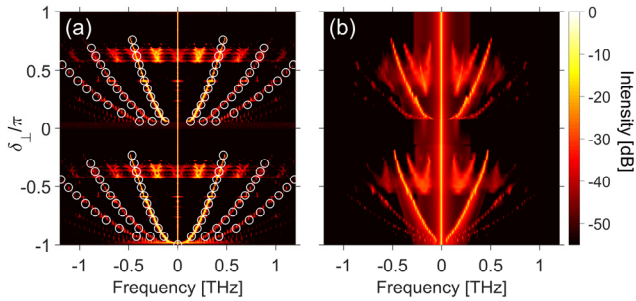


Fig. 2. Pseudo-color plots of (a) numerical and (b) experimental output spectra for various values of relative detuning δ_{\perp} , i.e., intra-cavity birefringence. Circles in (a) highlight how the position of the PMI sidebands match the theoretical predictions of Eq. (4). Driving power $X = 28$ and linear detuning $\Delta = 8$. Spectra are plotted as a function of frequency detuning from the central cw driving component.

To assess clearly the vector nature of the observed PMI sidebands, we have characterized the output spectrum obtained for

a relative detuning $\delta_{\perp} = 0.2\pi$ in terms of its polarization components that are parallel (blue curve) and orthogonal (red curve) to the driving field’s SOP, respectively [Fig. 3(b)]. The results clearly highlight that the first order PMI sidebands are mainly orthogonally polarized to the driving field, with an extinction-ratio better than 20 dB. In contrast, higher order sidebands exhibit alternating SOPs. This behavior is similar to that observed in conventional isotropic PMI experiments performed in single-pass fiber segments [19].

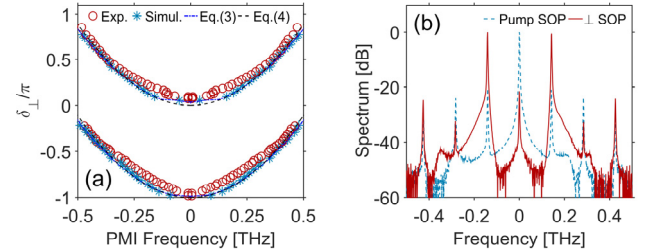


Fig. 3. (a) Optimum frequency (Ω_{opt}) of the first-order PMI sidebands as a function of the relative detuning δ_{\perp} . Experimental results (red circles) are compared with numerical simulations (blue stars) as well as theoretical predictions of Eqs. (3)–(4) (blue and black dashed-lines, respectively). (b) Output spectrum for $\delta_{\perp} = 0.2\pi$ recorded after the output PBS and decomposed into polarization components parallel (blue) and orthogonal (red) to the driving SOP.

In addition to the spectral analysis shown in Figs. 2 and 3, we have also performed a temporal characterization of the intra-cavity intensity profile in the PMI regime using a 50-GHz bandwidth real-time oscilloscope. An example of measurement taken over a single cavity round-trip is shown in Fig. 4(a), where we can observe temporal oscillations at a frequency of about 15 GHz across our ns-long driving pulses. Here we have selected a value of δ_{\perp} slightly positive, and low enough for the PMI frequency to fit within the bandwidth of our oscilloscope and photodetectors. Also, observations are made in a polarization basis at 45° with respect to the SOP of the driving field and the PMI sidebands so as to mix the cw driving component with the PMI signal. In this way, the observed oscillations in intensity seen in both orthogonal polarization components (blue and red curves) are essentially proportional to the PMI sideband field *amplitude*. This provides maximal contrast and reveals oscillations at the actual PMI frequency [rather than its second harmonic, as $\cos^2(\Omega_{\text{opt}}) \propto 1+\cos(2\Omega_{\text{opt}})$]. The oscillations are also anti-correlated across the two components, which is typical of vector MI processes [17–20].

Additional insights into the temporal dynamics of intracavity PMI can be gained by monitoring the temporal intensity profile of the generated patterns round-trip by round-trip. An example of such measurement is shown in Fig. 4(b) in the form of a pseudo-color plot, showing data for 20 successive round-trips (bottom to top). The data was acquired single-shot by our oscilloscope as a long temporal sequence, which was then split into individual cavity round-trips. Here we only show a single polarization component, in the same basis as in Fig. 4(a), and δ_{\perp} is again small and positive. We can observe that the PMI pattern (here with a frequency of 27.5 GHz) is stable and repeats identically from round-trip to round-trip. In Fig. 4(c), we have also plotted the corresponding total intensity measured independently. This plot reveals hints of oscillations at twice the PMI frequency. Together with the low contrast (which is partly limited by the bandwidth of our

oscilloscope), this further confirms the vector nature of the observed patterns. Figures 4(d)–(e) display the results of a similar measurement but obtained for a relative detuning close to $-\pi$, i.e., close to anti-resonant conditions. In this case, as can be appreciated from the checkerboard-like pattern, the PMI pattern flips at every cavity round-trip, exhibiting a dynamics reminiscent of a round-trip period-doubled dynamics (P2) [27]. This behavior can be understood by noting that a relative detuning $\delta_{\perp} \sim \pm\pi$ makes the system acts as a half-wave plate, swapping the handedness of the circular polarization components at each round-trip, and leading to the observed flipping [28]. Interestingly, the total intensity [Fig. 4(e)] shows no sign of the periodic flipping, confirming that this behavior stems from a pure polarization dynamics.

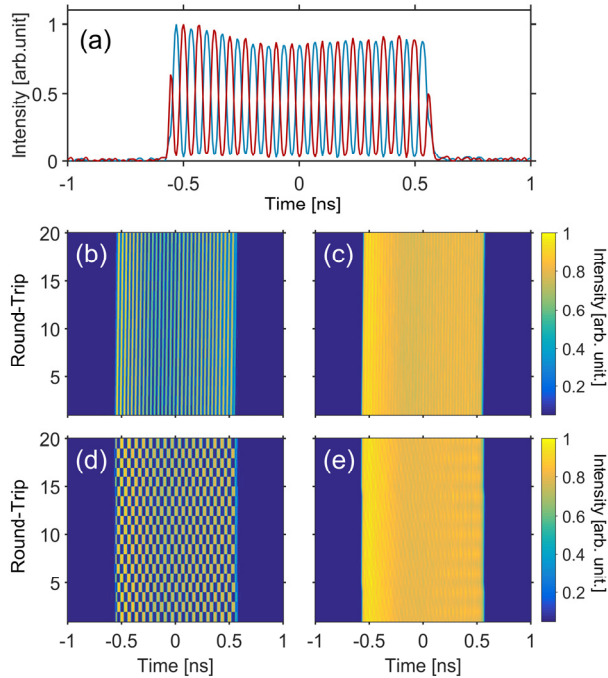


Fig. 4. (a) Typical experimentally measured temporal intensity profiles of both orthogonal polarization components (at 45° with respect to the driving and PMI sidebands SOPs) monitored at the output of the cavity for δ_{\perp} slightly positive (low PMI frequency, within the bandwidth of our detectors). (b) Round-trip by round-trip evolution (from bottom to top) of the temporal intensity profile at the output of our fiber cavity monitored on one of the polarization components (as used in panel (a)) for δ_{\perp} slightly above 0. (c) Corresponding total intensity (before the PBS). (d, e) Same as (b, c) but with δ_{\perp} slightly above $-\pi$.

In conclusion, we have reported the experimental observation of polarization modulation instability in a fiber Kerr resonator. It was shown that the phase matched PMI frequency is affected by the level of intra-cavity birefringence and can be well approximated with a simple equation, Eq. (4). Our experimental observations were performed in a 12-m long spun fiber ring cavity incorporating a polarization controller for accurate control of the level of birefringence. By means of real-time temporal characterizations, both steady and period-doubled (P2) behaviors have been observed. Experimental results were found to be in good agreement with theoretical predictions and numerical simulations based on a two-component Ikeda map. These results provide new insights into the control of dissipative MI in birefringent nonlinear resonators,

and establish birefringence as a potential new degree of freedom for frequency comb generation in normal dispersion Kerr resonators.

Funding. J. F. acknowledges the financial support from the Conseil Régional de Bourgogne Franche-Comté, APEX project and International Mobility Program as well as FEDER, Optiflex project. B. K. acknowledges support from the ANR (Project No. PIA2/ISITE-BFC, contract n° ANR-15-IDEX-03). We also acknowledge financial support from The Royal Society of New Zealand, in the form of Marsden Funding (18-UOA-310), as well as James Cook Fellowship (JCF-UOA1701, for S.C.).

Disclosures. The authors declare no conflicts of interest.

References

1. K. Tai, A. Hasegawa, and A. Tomita, Phys. Rev. Lett. **56**, 135 (1986)
2. G. P. Agrawal, *Nonlinear Fiber Optics* (5th ed., Academic Press, Oxford, 2013).
3. M. Nakazawa, K. Suzuki, and H. A. Haus, Phys. Rev. A **38**, 5193 (1988).
4. R. Vallée, Opt. Commun. **81**, 419 (1991).
5. M. Haeltermann, S. Trillo, and S. Wabnitz, Opt. Commun. **91**, 401 (1992).
6. S. Coen and M. Haelterman, Phys. Rev. Lett. **79**, 4139 (1997).
7. F. Copie, M. Conforti, A. Kudlinski, A. Mussot, and S. Trillo, Phys. Rev. Lett. **116**, 143901 (2016).
8. D. Ceolino, A. Bendahmane, J. Fatome, G. Millot, T. Hansson, D. Modotto, S. Wabnitz, and B. Kibler, Opt. Lett. **41**, 5462 (2016).
9. M. Conforti, A. Mussot, J. Fatome, A. Picozzi, S. Pitois, C. Finot, M. Haelterman, B. Kibler, C. Michel, and G. Millot, Phys. Rev. A **91**, 023823 (2015).
10. A. Bendahmane, J. Fatome, C. Finot, G. Millot, and B. Kibler, Opt. Lett. **42**, 251 (2017).
11. T. Hansson and S. Wabnitz, J. Opt. Soc. Am. B **32**, 1259 (2015).
12. F. Bessin, F. Copie, M. Conforti, A. Kudlinski, A. Mussot, and S. Trillo, Phys. Rev. X **9**, 041030 (2019).
13. S. Coen and M. Haelterman, Opt. Lett. **26**, 39 (2001).
14. F. Leo, S. Coen, P. Kockaert, S. P. Gorza, P. Emplit, and M. Haelterman, Nat. Photon. **4**, 471-476 (2010).
15. A. A. Savchenkov, A. B. Matsko, and L. Maleki, Nanophoton. **5**, 363 (2016).
16. P. Del'Haye, A. Schliesser, O. Arcizet, T. Wilken, R. Holzwarth, and T. J. Kippenberg, Nature **450**, 1214 (2007).
17. A. L. Berkhoer, and V. E. Zakharov, Sov. Phys. JETP **31**, 486 (1970).
18. P. Kockaert, M. Haelterman, S. Pitois, and G. Millot, Appl. Phys. Lett. **75**, 2873 (1999).
19. H. Zhang, M. Gilles, M. Guasoni, B. Kibler, A. Picozzi, and J. Fatome, J. Opt. Soc. Am. B **36**, 2445 (2019).
20. M. Haelterman, S. Trillo, and S. Wabnitz, J. Opt. Soc. Am. B **11**, 446 (1994).
21. A. Tonello, Opt. Quant. Electron. **32**, 1219-1238 (2000).
22. T. Hansson, M. Bernard, and S. Wabnitz, J. Opt. Soc. Am. B **35**, 835 (2018).
23. C. Bao et al, Opt. Lett. **44**, 1472 (2019).
24. L. Palmieri, A. Galatarossa, and T. Geisler, Opt. Lett. **35**, 2481 (2010).
25. I. P. Areshev, T. A. Murina, N. N. Rosanov and V. K. Subashiev, Opt. Commun. **47**, 414 (1983).
26. B. Garbin, J. Fatome, G.-L. Oppo, M. Erkintalo, S. G. Murdoch, and S. Coen, Phys. Rev. Res. **2**, 023244 (2020).
27. M. Haelterman and M. D. Tolley, Opt. Commun. **108**, 167 (1994).
28. J. Fatome, Y. Wang, B. Garbin, B. Kibler, A. Bendahmane, N. Berti, G.-L. Oppo, F. Leo, S. G. Murdoch, M. Erkintalo and S. Coen, in Advanced Photonics Congress, paper JTU6F.2 (2018).

Full References

1. K. Tai, A. Hasegawa, and A. Tomita, Observation of modulation instability in optical fibers, *Phys. Rev. Lett.* **56**, 135 (1986).
2. G. P. Agrawal, *Nonlinear Fiber Optics* (5th ed., Academic Press, Oxford, 2013).
3. M. Nakazawa, K. Suzuki, and H. A. Haus, "Modulational instability oscillation in nonlinear dispersive ring cavity," *Phys. Rev. A* **38**, 5193 (1988).
4. R. Vallée, "Temporal instabilities in the output of an all-fiber ring cavity," *Opt. Commun.* **81**, 419–426 (1991).
5. M. Haeltermann, S. Trillo, and S. Wabnitz, "Dissipative modulation instability in a nonlinear dispersive ring cavity," *Opt. Commun.* **91**, 401–407 (1992).
6. S. Coen and M. Haelterman, "Modulational instability induced by cavity boundary conditions in a normally dispersive optical fiber," *Phys. Rev. Lett.* **79**, 4139–4142 (1997).
7. F. Copie, M. Conforti, A. Kudlinski, A. Mussot, and S. Trillo, "Competing Turing and Faraday instabilities in longitudinally modulated passive resonators," *Phys. Rev. Lett.* **116**, 143901 (2016).
8. D. Ceoldo, A. Bendahmane, J. Fatome, G. Millot, T. Hansson, D. Modotto, S. Wabnitz, and B. Kibler, "Multiple four-wave mixing and Kerr combs in a bichromatically pumped nonlinear fiber ring cavity," *Opt. Lett.* **41**, 5462–5465 (2016).
9. M. Conforti, A. Mussot, J. Fatome, A. Picozzi, S. Pitois, C. Finot, M. Haelterman, B. Kibler, C. Michel, and G. Millot, "Turbulent dynamics of an incoherently pumped passive optical fiber cavity: Quasisolitons, dispersive waves, and extreme events," *Phys. Rev. A* **91**, 023823 (2015).
10. A. Bendahmane, J. Fatome, C. Finot, G. Millot, and B. Kibler, "Coherent and incoherent seeding of dissipative modulation instability in a nonlinear fiber ring cavity," *Opt. Lett.* **42**, 251–254 (2017).
11. T. Hansson and S. Wabnitz, "Frequency comb generation beyond the Lugiato-Lefever equation: multi-stability and super cavity solitons," *J. Opt. Soc. Am. B* **32**, 1259–1266 (2015).
12. F. Bessin, F. Copie, M. Conforti, A. Kudlinski, A. Mussot, and S. Trillo, "Real-Time Characterization of Period-Doubling Dynamics in Uniform and Dispersion Oscillating Fiber Ring Cavities," *Phys. Rev. X* **9**, 041030 (2019).
13. S. Coen and M. Haelterman, "Continuous-wave ultrahigh-repetition-rate pulse-train generation through modulational instability in a passive fiber cavity," *Opt. Lett.* **26**, 39–41 (2001).
14. F. Leo, S. Coen, P. Kockaert, S. P. Gorza, P. Emplit, and M. Haelterman, "Temporal cavity solitons in one-dimensional Kerr media as bits in an all-optical buffer," *Nat. Photon.* **4**, 471–476 (2010).
15. A. A. Savchenkov, A. B. Matsko, and L. Maleki, "On frequency combs in monolithic resonators," *Nanophoton.* **5**, 363–391 (2016).
16. P. Del'Haye, A. Schliesser, O. Arcizet, T. Wilken, R. Holzwarth, and T. J. Kippenberg, "Optical frequency comb generation from a monolithic microresonator," *Nature* **450**, 1214–1217 (2007).
17. A. L. Berkhoer, and V. E. Zakharov, "Self-excitation of waves with different polarizations in nonlinear media," *Sov. Phys. JETP* **31**, 486–490 (1970).
18. P. Kockaert, M. Haelterman, S. Pitois, and G. Millot, "Isotropic polarization modulational instability and domain walls in spun fibers," *Appl. Phys. Lett.* **75**, 2873–2875 (1999).
19. H. Zhang, M. Gilles, M. Guasoni, B. Kibler, A. Picozzi, and J. Fatome, "Isotropic polarization modulational instability in single-mode conventional telecom fibers," *J. Opt. Soc. Am. B* **36**, 2445–2451 (2019).
20. M. Haelterman, S. Trillo, and S. Wabnitz, "Polarization multistability and instability in a nonlinear dispersive ring cavity," *J. Opt. Soc. Am. B* **11**, 446–456 (1994).
21. A. Tonello, "The role of birefringence in modulation instability fiber ring resonators," *Opt. Quant. Electron.* **32**, 1219–1238 (2000).
22. T. Hansson, M. Bernard, and S. Wabnitz, "Modulational instability of nonlinear polarization mode coupling in microresonators," *J. Opt. Soc. Am. B* **35**, 835–841 (2018).
23. C. Bao et al, "Orthogonally polarized frequency comb generation from a Kerr comb via cross-phase modulation," *Opt. Lett.* **44**, 1472–1475 (2019).
24. L. Palmieri, A. Galtarossa, and T. Geisler, "Distributed characterization of bending effects on the birefringence of single-mode optical fibers," *Opt. Lett.* **35**, 2481–2483 (2010).
25. I. P. Areshev, T. A. Murina, N. N. Rosanov and V. K. Subashiev, "Polarization and amplitude optical multistability in a nonlinear ring cavity," *Opt. Commun.* **47**, 414–419 (1983).
26. B. Garbin, J. Fatome, G.-L. Oppo, M. Erkintalo, S. G. Murdoch, and S. Coen "Asymmetric balance in symmetry breaking," *Phys. Rev. Res.* **2**, 023244 (2020).
27. M. Haelterman and M. D. Tolley, "Pure polarization period-doubling instability in a Kerr-type nonlinear ring cavity," *Opt. Commun.* **108**, 167–175 (1994).
28. J. Fatome, Y. Wang, B. Garbin, B. Kibler, A. Bendahmane, N. Berti, G.-L. Oppo, F. Leo, S. G. Murdoch, M. Erkintalo, and S. Coen, "Flip-flop polarization domain walls in a Kerr resonator", in *Advanced Photonics Congress*, paper JT6F.2 (2018).